ACS APPLIED MATERIALS & INTERFACES

www.acsami.org

Research Article

Magnetic Particle Spectroscopy for Detection of Influenza A Virus Subtype H1N1

Kai Wu,* Jinming Liu, Renata Saha, Diqing Su, Venkatramana D. Krishna, Maxim C.-J. Cheeran, and Jian-Ping Wang*

Cite This: *ACS Appl. Mater. Interfaces* 2020, 12, 13686−13697

Read Online

ACCESS | Metrics & More | Article Recommendations | Supporting Information

ABSTRACT: Magnetic nanoparticles (MNPs) with proper surface functionalization have been extensively applied as labels for magnetic immunoassays, carriers for controlled drug/gene delivery, tracers and contrasts for magnetic imaging, etc. Here, we introduce a new biosensing scheme based on magnetic particle spectroscopy (MPS) and the self-assembly of MNPs to quantitatively detect H1N1 nucleoprotein molecules. MPS monitors the harmonics of oscillating MNPs as a metric for the freedom of rotational process, thus indicating the bound states of MNPs. These harmonics can be readily collected from nanogram quantities of iron oxide nanoparticles within 10 s. The H1N1 nucleoprotein molecule hosts multiple different epitopes that forms binding sites for many IgG polyclonal antibodies. Anchoring IgG polyclonal antibodies onto MNPs triggers the cross-linking between MNPs and H1N1 nucleoprotein molecules, thereby forming MNP self-assemblies. Using MPS and the self-assembly of MNPs, we were able to detect as low as 44 nM (4.4 pmole) H1N1 nucleoprotein. In addition, the morphologies and the hydrodynamic sizes of the MNP self-assemblies are characterized to verify the MPS results. Different MNP self-assembly models such as classical cluster, open ring tetramer, and chain model as well as multimers (from dimer to pentamer) are proposed in this paper. Herein, we claim the feasibility of using MPS and the self-assembly of MNPs as a new biosensing scheme for detecting ultralow concentrations of target biomolecules, which can be employed as rapid, sensitive, and wash-free magnetic immunoassays.

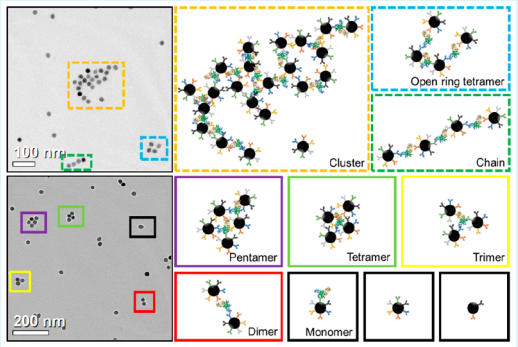

KEYWORDS: *magnetic nanoparticles, influenza A virus, self-assembly, magnetic particle spectroscopy, wash-free magnetic immunoassay*

1. INTRODUCTION

Influenza A virus (IAV) infects many vertebrates including humans and is responsible for seasonal epidemics of acute respiratory illness known as influenza or flu. IAV poses a significant public health concern that causes substantial morbidity and mortality and has the ability to cause worldwide pandemics.[1,2] According to the World Health Organization (WHO), influenza viruses are responsible for 290,000 to 650,000 deaths annually.[3] Rapid, accurate, and sensitive methods for early diagnosis of IAV infections are critical for rapid initiation of antiviral therapy to control infection and to reduce the impact of possible influenza pandemics.

IAV nucleoprotein is a basic protein that binds to viral RNA along with polymerase and is the most abundant component of the ribonucleoprotein complex.[4] Each ribonucleoprotein consists of one genomic RNA segment associated with a single trimeric polymerase complex and multiple nucleoprotein monomers.[5,6] In addition to binding single stranded RNA, IAV nucleoprotein has been shown to self-assemble to form large oligomeric complexes.[7] IAV nucleoprotein is well conserved among different IAV strains isolated from different host species with an amino acid difference of less than 11%.[8] These properties make IAV nucleoprotein a good target for detection of multiple IAV subtypes without the risk of missing detection of new variants due to mutation in the virus.[9] Moreover, IAV nucleoprotein has been used as a target in other studies, including several antigen detection tests currently approved for use in human clinical samples.[10,11]

The conventional detection schemes of IAV can be divided into several categories based on the type of assays employed. Immunofluorescence assays use either direct or indirect fluorescent antibody staining techniques to detect IAV. The signal can be read out through fluorescent microscopes with clinical sensitivities of 60−80% and analytical sensitivities in the order of nM.[12] However, they are unable to distinguish different IAV subtypes.[13] Serological tests such as hemagglutination inhibition assays, microneutralization or virus neutralization assays, and enzyme linked immunosorbent assays (ELISA) are the most commonly used techniques to detect

Received: January 14, 2020
Accepted: March 9, 2020
Published: March 9, 2020

https://dx.doi.org/10.1021/acsami.0c00815
ACS Appl. Mater. Interfaces 2020, 12, 13686−13697

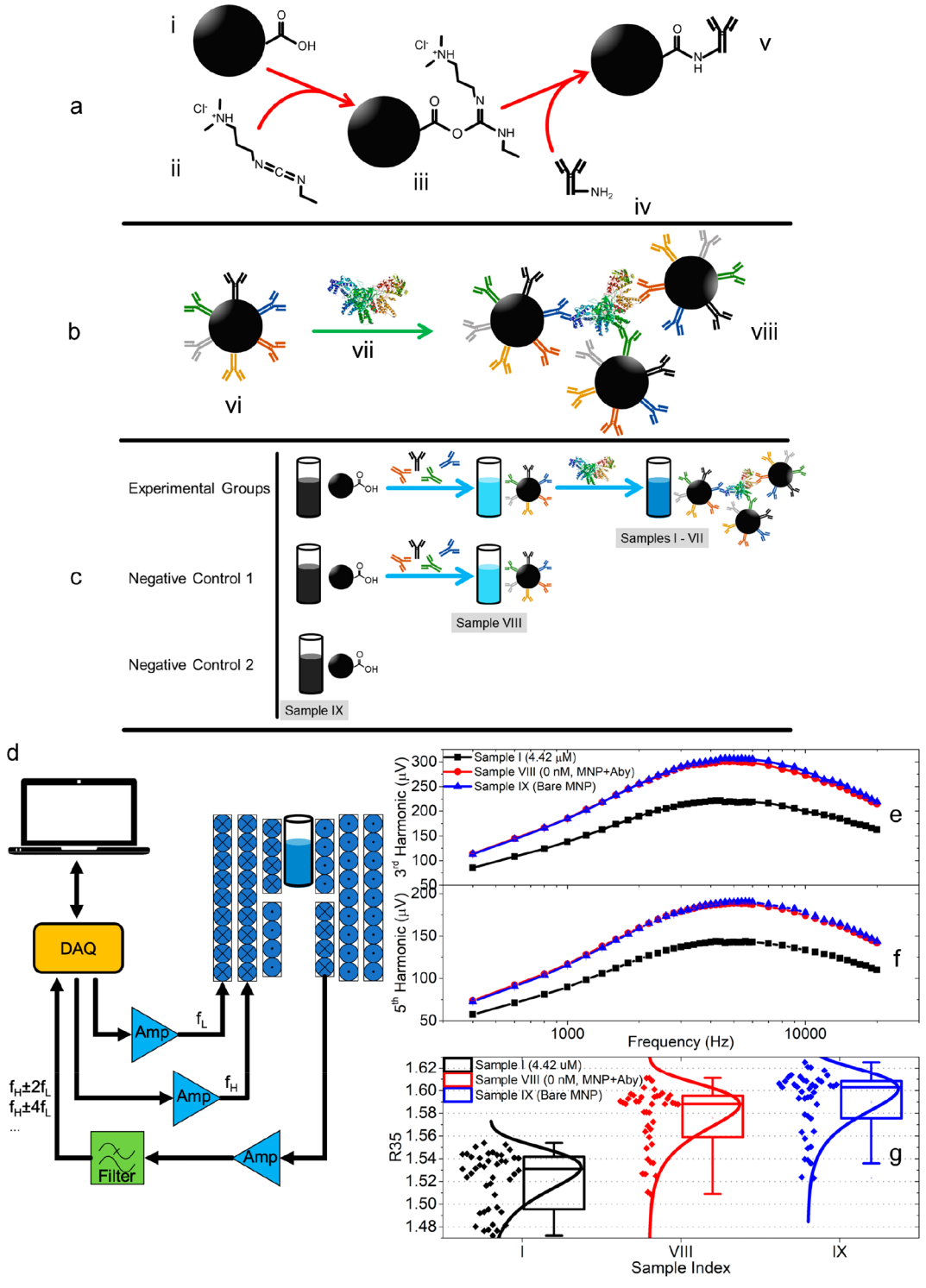

Figure 1. (a) EDC (carbodiimide) cross-linking reaction scheme. (i) SHP-25 MNP with a carboxylic acid group; (ii) EDC cross-linker; (iii) O-acylisourea active ester (unstable) on MNP; (iv) the polyclonal IgG with a primary amine group; (v) the reaction of O-acylisourea with the amine from IgG forms a stable amide bond on MNP. (b) Schematic view of the self-assembly of MNPs through proper choice of IgG polyclonal antibodies and target antigen hosting multiple different epitopes. vi) SHP-25 MNP surface conjugated with IgG polyclonal antibodies; vii) the H1N1 nucleoprotein (AAM75159.1; Met1-Gly490) possessing multiple different epitopes that allows a number of IgG polyclonal antibodies to bind; viii) the final product of the self-assembled MNPs. (c) Sample preparation flowcharts of the experimental and negative control groups. Nine MNP samples are prepared: sample indexes I–VII are MNP-antibody complexes in the presence of different concentrations of the H1N1 nucleoprotein; sample index VIII is an MNP-antibody complex in the absence of the H1N1 nucleoprotein (denoted as '0 nM (MNP+Aby)' in this paper); sample index IX is bare MNP suspension (denoted as "Bare MNP" in this paper). The details of samples I–IX are listed in Table S3 of the Supporting Information. (d) Schematic view of MPS system setups. (e) and (f) are the third and the fifth harmonics along varying driving field frequencies (only samples I, VIII, and IX are plotted) collected by the MPS system. (g) Boxplots of the harmonic ratios (R35) collected from samples I, VIII, and IX. Note that parts (a)–(c) are not drawn to scale.

https://dx.doi.org/10.1021/acsami.0c00815
ACS Appl. Mater. Interfaces 2020, 12, 13686–13697

influenza virus-specific antibody responses, but they usually need paired samples with strict requirements of the sample collection time.[14] Nucleic acid-based assays such as reverse transcription-polymerase chain reaction (RT-PCR) are based on the detection of DNA/RNA sequences of the viruses. Apart from the fact that a long reaction time (1−8 h) is required, RT-PCR is one of the most expensive testing techniques.[15] To cut down the time of detection, rapid influenza diagnostic tests (RIDTs) have also been developed with RT-PCR and ELISA as the two gold standards.[16,17] Although the total testing time is less than 30 min with high specificities (95−99%), the clinical sensitivities of the RIDTs are lower than other techniques (10−70%), and false negative results should be considered.[18,19] Giant magnetoresistive (GMR) biosensors have also been reported for the detection of IAV both in lab-based and point-of-care platforms.[20−22] However, this technique is limited by the complexity of nanofabricating the GMR sensors as well as the cost per chip/test.

Magnetic particle spectroscopy (MPS), a novel measurement tool that is closely related to magnetic particle imaging (MPI), has emerged in recent years as an alternative to the aforementioned techniques and is gaining increasing attention in the area of volumetric-based bioassays.[23−27] In MPS, also called 0D MPI, oscillating magnetic fields periodically drive magnetic nanoparticles (MNPs) into saturated states where the magnetic responses contain not only the fundamental driving field frequencies but also a series of harmonic frequencies. These harmonics are very useful metrics for characterizing the MNP ferrofluids such as the viscosity and temperature of the solution as well as the conjugations of chemical compounds on the MNPs.[27−32] Nowadays, with the ease of fabricating and surface-functionalizing MNPs, MNPs functionalized with ligands, DNA, RNA, and protein molecules can be readily applied as probes, labels, contrasts, and tracers for different bioassays.[27,32−40] Unlike the surface-based biosensing platforms (ELISA, GMR, Hall effect sensors, etc.) that directly detect individual target objects near the sensing elements, the volumetric-based biosensing platforms measure the analytical signals that directly come from the entire detection volume, making the bioassays simple and fast.[41−45] Representative examples of volumetric-based biosensors are the nuclear magnetic resonance (NMR) devices and the magnetic susceptometers.[46−52] MPS is one type of volumetric-based biosensing platform where the MNPs are acting as the minisensing probes, and their dynamic magnetic responses are used as metrics for the characterization of target analytes from the fluidic samples.[53−57]

In this current work, we report the MPS-based bioassay platform as a rapid, sensitive, and wash-free method for the detection of the H1N1 nucleoprotein. It should be noted that the MPS method reported in this paper is different from the standard MPS where there is one sinusoidal magnetic field to excite MNPs.[23−25] Herein, a dual driving field based MPS modality is used (see Figure 1(d) and Section 2.2). Due to the IgG antibodies anchored on the MNPs, cross-linking takes place between MNPs and the H1N1 nucleoprotein which forms MNP clusters (see Figure 1(b)). Characterization of these MNP clusters reveals their controlled formation, and hence in the upcoming sections we have referred to them as MNP "self-assemblies". The third and the fifth harmonics along with the third over the fifth harmonic ratios (R35) can be used as metrics for the characterization of target analyte concentrations from fluidic samples. These harmonics can be detected from nanogram quantities of iron oxide MNPs within 10 s. We show that the H1N1 nucleoprotein can be detected with high sensitivity (as low as 44 nM or 4.4 pmole) using this detection scheme, which is comparable to the analytical sensitivity of fluorescent assays. By combining MPS technology and the self-assembly of MNPs, we are able to achieve rapid, sensitive, and wash-free magnetic bioassays. Furthermore, this detection scheme utilizing the self-assembly of MNPs is suitable for detecting and quantifying a wide range of biomarkers/analytes.

2. MATERIALS AND METHODS

2.1. Materials. The recombinant Influenza A virus (A/Puerto Rico/8/34/Mount Sinai (H1N1)) nucleoprotein (AAM75159.1; Met1-Gly490) was purchased from Sino Biological Inc. (Catalog# 11675-V08B). It comprises of 501 amino acids and has a predicted molecular mass of 56.6 kDa. The H1N1 nucleoprotein is provided as a lyophilized powder from sterile 60 mM Tris and 500 mM NaCl, pH 7.4 and stored at −20 °C under sterile conditions before usage. The lyophilized H1N1 nucleoprotein powder is reconstituted in DI water to prepare a stock solution of 0.25 mg/mL (4.42 μM). The Influenza A nucleoprotein specific polyclonal IgG is produced in rabbits immunized with purified, recombinant Influenza A nucleoprotein (Catalog# 11675-V08B; AAM75159.1; Met1-Gly490). This rabbit IgG polyclonal antibody purchased from Sino Biological Inc. (Catalog# 11675-T62) is provided as a liquid solution with a measured concentration of 2 mg/mL and stored at −20 °C before usage. The rabbit polyclonal IgG is diluted in PBS to a desired concentration of 5 μg/mL. The MNPs, with an average particle magnetic core size of 25 nm, concentration of 0.29 nmol/mL nanoparticles (5 mg/mL Fe), and suspended in DI water containing 0.02% sodium azide, were purchased from Ocean NanoTech Inc. (Catalog# SHP-25). They are water-soluble iron oxide nanoparticles coated with a monolayer of oleic acid and a monolayer of amphiphilic polymer, their reactive group is carboxylic acid, and their zeta potential is between −35 mV and −15 mV. EDC (1-ethyl-3-(3-(dimethylamino)propyl)carbodiimide hydrochloride, $C_8H_{17}N_3$·HCl) was purchased from Thermo Fisher Scientific (Catalog# 22980). It is a water-soluble carbodiimide cross-linker that activates the carboxyl groups on MNPs for spontaneous reaction with primary amines from rabbit IgG polyclonal antibodies, enabling stable antibody conjugation. The EDC powder is dissolved in DI water to a desired concentration of 10 mg/mL before immediate use. MES (2-(*N*-morpholino)ethanesulfonic acid, $C_6H_{13}NO_4S$, Prod. No. M3671), Trizma hydrochloride (tris(hydroxymethyl)aminomethane hydrochloride, $NH_2C(CH_2OH)_3$·HCl, Prod. No. T5941), and Phosphate Buffered Saline (PBS, Prod. No. 79378) were purchased from Sigma-Aldrich. The MES powder is dissolved in DI water to a desired concentration of 25 mM, pH 6.0. Trizma hydrochloride powder is dissolved in DI water to a desired concentration of 100 mM, pH 7.4.

2.2. Magnetic Particle Spectroscopy (MPS) System Setups. The lab-based MPS system setups can be found in the Supporting Information Note S1, and the signal chain is shown in Figure 1(d). A laptop installed with LabVIEW sends commands to the Data Acquisition Card (DAQ, NI USB-6289) to generate two sinusoidal waves, which are amplified by two Instrument Amplifiers (IA, HP 6824A). These amplified sinusoidal waves are sent to the primary and secondary coils to produce oscillating magnetic fields: one with frequency f_L = 10 Hz and amplitude A_L = 170 Oe, the other with frequency f_H varying from 400 Hz to 20 kHz and amplitude A_H = 17 Oe. One pair of differently wound pick-up coils (600 windings clockwise and 600 windings counterclockwise) senses the induced magnetic responses from MNPs and sends back to DAQ. The response signals at combinatorial frequencies $f_H \pm 2f_L$ (the third harmonics) and $f_H \pm 4f_L$ (the fifth harmonics) are extracted and analyzed.

2.3. Conjugating IgG Polyclonal Antibodies on MNPs. To immobilize rabbit IgG polyclonal antibodies onto MNPs, the zero-

https://dx.doi.org/10.1021/acsami.0c00815
ACS Appl. Mater. Interfaces 2020, 12, 13686−13697

Scheme 1[a]

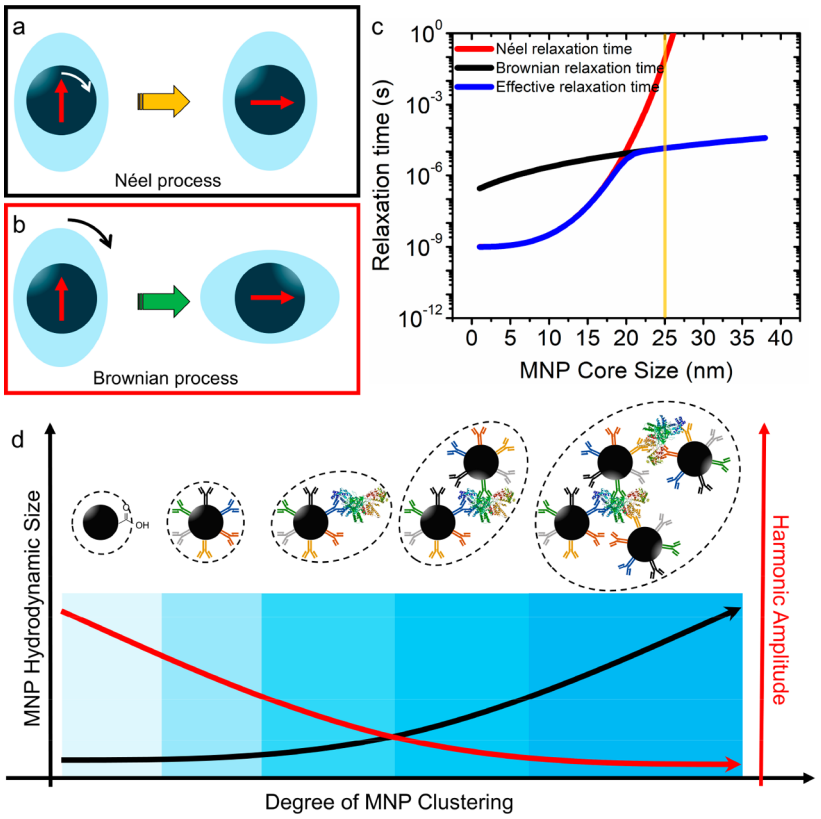

[a](a) The Néel process is the rotation of magnetic moment inside the stationary MNP. (b) The Brownian process is the rotation of the entire MNP along with its magnetic moment. (c) The Néel, Brownian, and effective relaxation times are depicted as a function of iron oxide MNP core size, assuming MNPs are dispersed in a solution with viscosity η = 1 cP and temperature T = 300 K. Assuming MNPs with anisotropy constant K_u = 90000 erg/cm^3, coated with 4 nm polymer layer. The vertical orange line highlights that the Brownian process is the dominating relaxation mechanism for iron oxide MNPs with a core size of 25 nm. The magnetic relaxation time models can be found in Supporting Information Note S2. (d) As the degree of MNP self-assembly increases in the presence of the H1N1 nucleoprotein, the average hydrodynamic size of particles (MNPs and MNP self-assemblies) increases, and as a result, the measured harmonic amplitude decreases. The dashed black lines represent the hydrodynamic sizes of MNPs and MNP self-assemblies. Note that parts (a), (b), and (d) are schematics and are not drawn to scale.

length carbodiimide cross-linker EDC is used to couple the carboxyl groups from MNPs to the primary amines from IgG. As shown in Figure 1(a):i–iii, EDC reacts with the carboxylic acid group from MNP to form an *O*-acylisourea active ester that can be easily displaced by nucleophilic attack from the primary amino group on IgG. In this step, a 1.5 mL microcentrifuge tube containing 200 μL of 0.29 nmol/mL SHP-25 MNP suspension is mixed with 200 μL of 25 mM MES and 10 μL of 10 mg/mL EDC, and the mixture reacted at room temperature for 15 min with continuous mixing. Then, 100 μL of 5 μg/mL polyclonal IgG is added to the suspension, and the mixture reacted at room temperature for 2.5 h with continuous mixing. As is shown in Figure 1(a):iii–v, the primary amine from IgG forms an amide bond with the original carboxyl group, and an EDC byproduct is released as a soluble urea derivative (not shown in the figure). Hereafter, 100 μL of 100 mM Trizma hydrochloride buffer is added to the suspension, and the mixture reacted at room temperature for 30 min with continuous mixing to quench the EDC activation reaction. The MNP and IgG antibody complexes (denoted as 'MNP+Aby' in this paper) are formed, the unconjugated IgG polyclonal antibodies are removed by ultracentrifuging the MNP ferrofluid at 11 000 rpm, acceleration 11 200g, for 45 min (PowerSpin BX Centrifuge), then the supernatant is removed, and the remaining MNP+Aby complexes are resuspended in 1% BSA in PBS to a total volume of 200 μL (in order to maintain the original concentration of 0.29 nmol/mL nanoparticles). This wash step is repeated three times to thoroughly remove the unconjugated IgG polyclonal antibodies. Using the same method, eight samples each containing 100 μL of 0.29 nmol/mL MNP+Aby complexes in 1% BSA in PBS buffer are prepared (labeled as samples I–VIII). The as-prepared MNPs anchored with rabbit IgG polyclonal antibodies are ready to be used for bioassays and can be stored at 2 °C–8 °C under sterile conditions for one month without detectable loss of magnetic properties of MNPs and activity of IgG. This test kit containing microliter volume surface functionalized MNPs allows for future field bioassays along with a portable MPS platform.

2.4. The Experimental and Control Groups. As shown in Figure 1(c), to the as-prepared MNP-IgG samples I–VII was added 100 μL of the H1N1 nucleoprotein of varying concentrations (from 4.42 μM down to 44 nM as listed in Table S3 in the Supporting Information). To sample VIII was added 100 μL of PBS buffer (instead of antigen) as negative control group #1 (denoted as '0 nM (MNP+Aby)' in this paper). Sample IX containing 100 μL of 0.29 nmol/mL SHP-25 MNP and 100 μL of PBS buffer (without antibody or the H1N1 nucleoprotein) is prepared as negative control group #2 (denoted as "Bare MNP" in this paper). Samples I–IX are incubated at room temperature for 2 h with continuous mixing to allow the cross-linking of MNPs and H1N1 nucleoprotein molecules, followed by storage at 2 °C–8 °C under sterile conditions before the MPS measurements.

3. RESULTS AND DISCUSSION

3.1. Self-Assembly of MNPs. Different degrees of MNP self-assemblies (here different degrees indicate the number and average sizes of MNP self-assemblies) are formed in samples

https://dx.doi.org/10.1021/acsami.0c00815
ACS Appl. Mater. Interfaces 2020, 12, 13686–13697

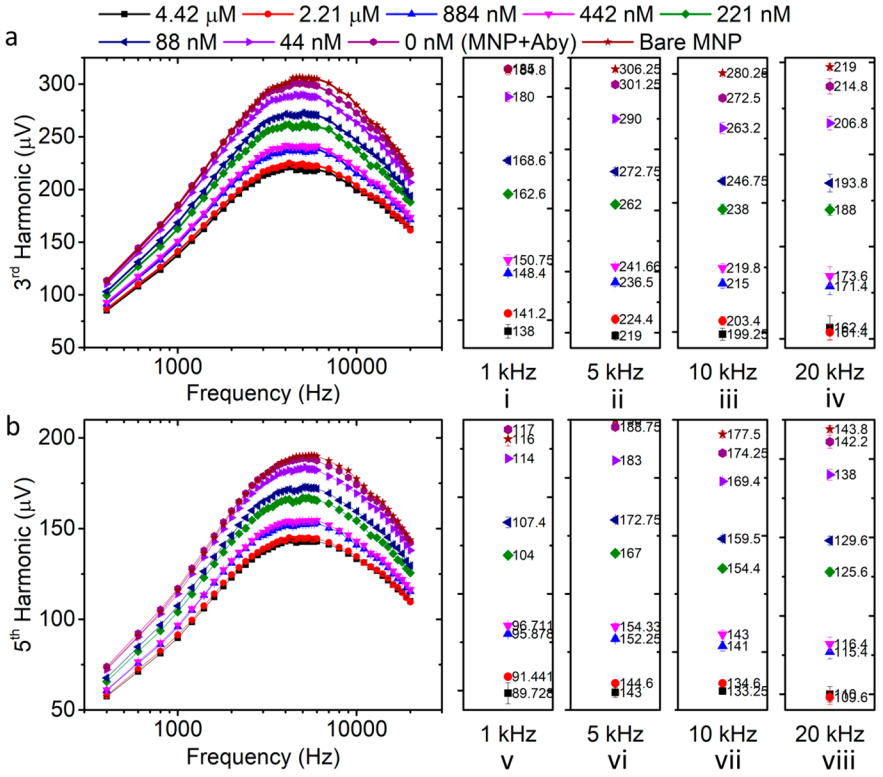

Figure 2. (a, b) MPS measurements of the third and the fifth harmonics from samples I−IX at varying driving field frequencies from 400 Hz to 20 kHz. The insets in (i)−(iv) highlight the third harmonic amplitudes measured at 1 kHz, 5 kHz, 10 kHz, and 20 kHz, respectively. Insets (v)−(viii) highlight the fifth harmonic amplitudes measured at 1 kHz, 5 kHz, 10 kHz, and 20 kHz, respectively. The error bar represents standard deviation from one single test. The third and the fifth harmonic amplitudes from part (a):i−iv and part (b):v−viii are listed in Tables S1 and S2 in the Supporting Information.

I−VII since the H1N1 nucleoprotein molecule has multiple epitopes recognized by polyclonal antibodies (see Figure 1(b)). As a result, each H1N1 nucleoprotein is bound to more than one MNP. On the other hand, each MNP functionalized with multiple IgG polyclonal antibodies can bind with multiple H1N1 nucleoprotein molecules. Thus, the cross-linking of MNPs and H1N1 nucleoproteins leads to different degrees of MNP self-assemblies depending on the number/concentration of H1N1 nucleoproteins in the MNP ferrofluid. It is proved by the Dynamic Light Scatter (DLS) results in Section 3.6 that the hydrodynamic sizes of the MNPs increase as the concentration of H1N1 nucleoproteins increases. A larger particle hydrodynamic size of the indicates a higher degree of MNP self-assembly. The average particle hydrodynamic sizes of samples II (2.21 μM), IV (442 nM), VI (88 nM), VIII (0 nM, MNP+Aby), and IX (0 nM, bare MNP) are 58.8 nm, 51.7 nm, 48.7 nm, 48.4 nm, and 46.3 nm, respectively.

3.2. Detection of the H1N1 Nucleoprotein via MPS and Magnetic Relaxation Dynamics. When the MNPs are suspended in a solution under oscillating magnetic fields, there are two mechanisms governing the rotation of magnetic moments in response to the magnetic fields (see Scheme 1(a) and (b)). One is the intrinsic Néel process (rotating magnetic moment inside the stationary MNP), and the other is the extrinsic Brownian process (rotating the entire MNP along with its magnetic moment). In principle, the joint effects of Néel and Brownian relaxation mechanisms contribute to the macroscopic magnetic response of the MNP ferrofluid sample subjected to external oscillating magnetic fields. Herein, we use the SHP-25 MNPs with an average core diameter of 25 nm, where the Brownian process is the dominating relaxation mechanism and thus determines the macroscopic magnetic responses of MNPs (in this case the effect of the Néel process is negligible, see Scheme 1(c)). For these Brownian process-dominated MNPs, their macroscopic magnetic responses are directly related to the overall hydrodynamic sizes.

MPS-based bioassay uses the harmonics of oscillating MNPs as a metric for the freedom of rotational process, thus indicating the degree of MNP self-assembly. In the presence of H1N1 nucleoprotein molecules, the polyclonal IgG functionalized MNPs can bind to one nucleoprotein molecule or cross-link to multiple nucleoprotein molecules, thus, forming MNP self-assemblies (see Scheme 1(d)). Such an interaction leads to an increased hydrodynamic size of the MNPs, resulting in an increased Brownian relaxation time, which is monitored by the MPS. The third and the fifth harmonics are immediately recorded at $f_H \pm 2f_L$ and $f_H \pm 4f_L$. In addition, the ratio of the third over the fifth harmonic (R35) is used as an MNP quantity-independent metric for the detection of the H1N1 nucleoprotein. Herein, we report using the third and the fifth harmonics along with the third over the fifth harmonic ratio (R35) as metrics for the characterization of target analyte concentrations from fluidic samples (see example plots in Figure 1(e)−(g)). The harmonic amplitudes and harmonic ratio R35 models are given in Supporting Information Notes S6 and S7.

3.3. The Third and the Fifth Harmonics as Metrics for the Detection of the H1N1 Nucleoprotein. The magnetic responses of MNPs from the as-prepared samples I−IX are monitored and recorded by our lab-based MPS system. One

https://dx.doi.org/10.1021/acsami.0c00815
ACS Appl. Mater. Interfaces 2020, 12, 13686−13697

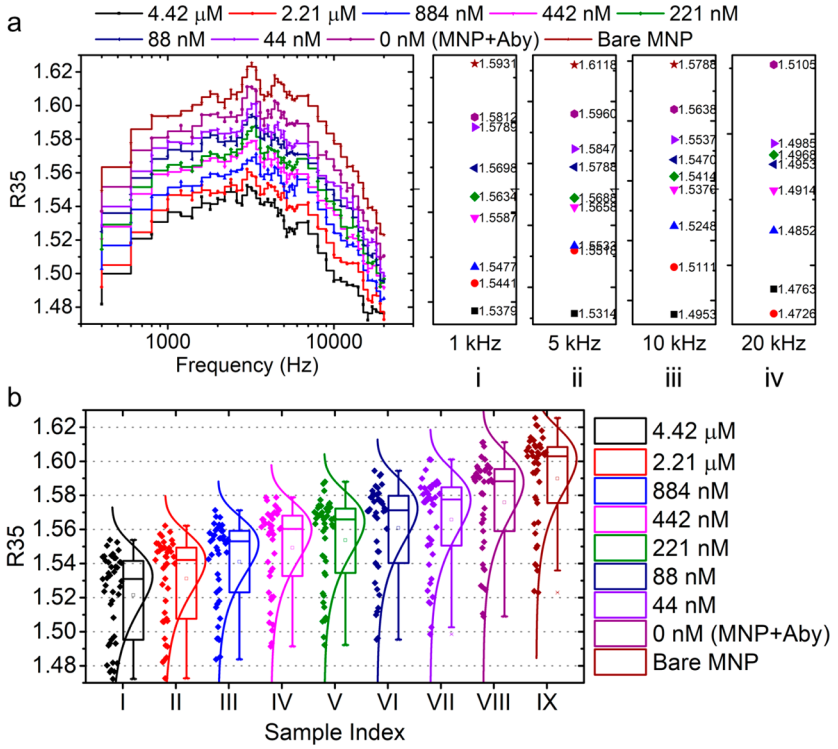

Figure 3. MPS measurements of the ratio of the third over the fifth harmonics (R35) from samples I–IX. (a) Harmonic ratios, R35, from samples I–IX as we vary the driving field frequencies from 400 Hz to 20 kHz. Insets (i)–(iv) highlight the R35 measured at 1 kHz, 5 kHz, 10 kHz, and 20 kHz, respectively. (b) Boxplot of R35 from samples I–IX. The first quartile (Q1, 25th percentile), median (Q2, 50th percentile), and third quartile (Q3, 75th percentile) values from samples I–IX are summarized in Table 1. The R35 heatmap of samples I–IX is reported in Notes S8 in the Supporting Information.

negative control group, group #1 (sample VIII, see Figure 1(c)), is added to this experiment to validate the selectivity in detection of the target biomarker, i.e., the H1N1 nucleoprotein. The other negative control group, group #2 (sample IX, see Figure 1(c)), is added to verify the efficiency of anchoring rabbit IgG polyclonal antibodies on MNPs.

The description of our lab-based MPS system setup can be found in Supporting Information Note S1, and a representative signal chain is shown in Figure 1(d). The frequency f_H of the high-frequency driving field is swept from 400 Hz to 20 kHz, and the frequency of the low-frequency driving field is set at 10 Hz. The amplitudes of the high- and low-frequency driving fields are set at 17 and 170 Oe, respectively. The sampling rate is set at 500 kHz. In each MPS measurement, the background noise floor is collected for 5 s followed by inserting the sample for another 5 s of data collection. The third and the fifth harmonics from the magnetic responses of MNPs are reconstructed from the signal and background noise.

As shown in Figure 2, according to Faraday's Law of Induction and the Langevin model (see Notes S3–S6 in the Supporting Information), the amplitudes of the third and the fifth harmonics are modulated by the driving field frequency f_H. With increasing concentration/quantity of the H1N1 nucleoprotein in the samples, MNPs are likely to form larger self-assemblies, and as a result, the Brownian relaxation time (as well as the effective relaxation time) increases. This increased relaxation time causes an increased phase lag (see Notes S4 in the Supporting Information) between the magnetic moments of MNPs and the external oscillating magnetic fields.

The amplitudes of the third and the fifth harmonics from samples I–IX are summarized in Figure 2(a) and (b), which shows a clear trend that at all driving field frequencies, the samples with higher concentrations of the H1N1 nucleoprotein, yield weaker magnetic responses (i.e., smaller harmonic amplitudes). This is due to the following facts: 1) larger MNP self-assemblies are formed in the presence of higher concentration/quantity of the H1N1 nucleoprotein; 2) the Brownian processes of MNPs that are cross-linked in the self-assemblies are blocked (i.e., larger hydrodynamic size as shown in Scheme 1(d)); and 3) the magnetic moments of these "trapped" MNPs fail to align with the external magnetic fields, thus, weaker dynamic magnetic responses are observed from these samples. This larger hydrodynamic size causes larger phase delay between the magnetic responses and the driving fields. As a result, the detected harmonic amplitudes drop (see Supporting Information Notes S6). In addition, the driving field frequency also modulates the harmonic amplitudes in a way that, when the driving field frequency is below 5 kHz, the phase delay to driving field is negligible and the harmonic amplitudes monotonically increase as f_H increases. However, as we further increase f_H beyond 5 kHz, the phase delay becomes significant, and it increases as f_H increases. Consequently, we see the harmonic amplitudes monotonically decrease as f_H increases beyond 5 kHz. The measured harmonic amplitudes arranged from lowest to highest are I (4.42 μM) < II (2.21 μM) < III (884 nM) < IV (442 nM) < V (221 nM) < VI (88 nM) < VII (44 nM) < VIII (0 nM, MNP+Aby) < IX (0 nM, bare MNP). Figure 2(a):i–iv and Figure 2(a):v–viii highlight the amplitudes of the third and the fifth harmonics at driving field frequencies of 1 kHz, 5 kHz, 10 kHz, and 20 kHz,

https://dx.doi.org/10.1021/acsami.0c00815
ACS Appl. Mater. Interfaces 2020, 12, 13686–13697

Table 1. 25th, 50th, and 75th Percentile R35 Values of 9 Samples in the Boxplot from Figure 3(b)

sample index	I	II	III	IV	V	VI	VII	VIII	IX
25th percentile (Q1)	1.541	1.549	1.559	1.568	1.573	1.580	1.585	1.595	1.610
50th percentile (Q2)	1.531	1.542	1.553	1.560	1.566	1.571	1.578	1.588	1.603
75th percentile (Q3)	1.495	1.508	1.523	1.533	1.534	1.540	1.550	1.559	1.576

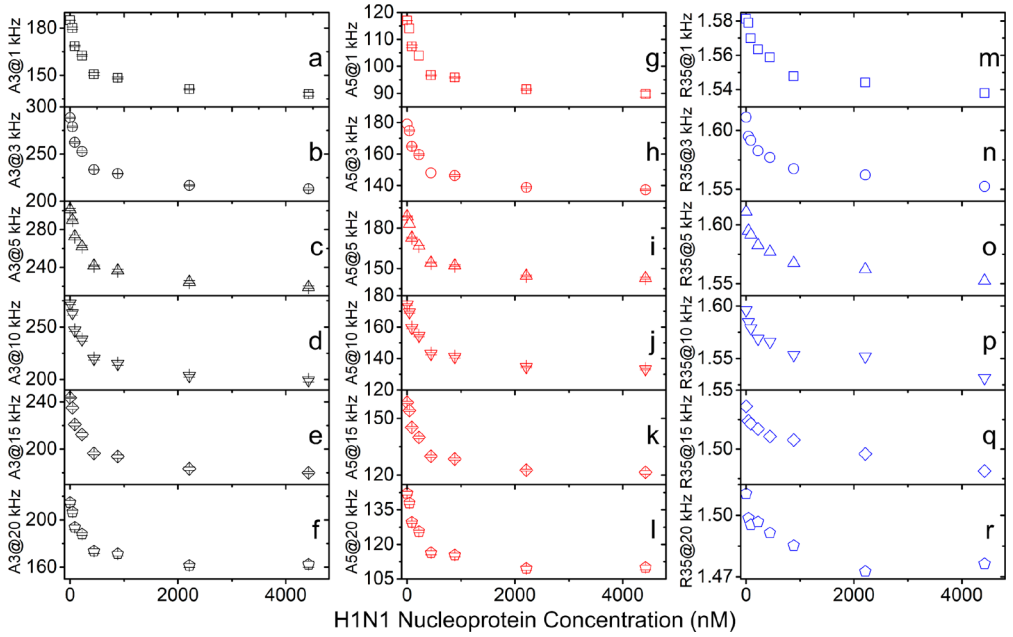

Figure 4. (a)−(f) are the amplitudes of the third harmonics from samples I−VIII at driving field frequencies of (a) 1 kHz, (b) 3 kHz, (c) 5 kHz, (d) 10 kHz, (e) 15 kHz, and (f) 20 kHz, respectively. (g)−(l) are the amplitudes of the fifth harmonics from samples I−VIII at driving field frequencies of (g) 1 kHz, (h) 3 kHz, (i) 5 kHz, (j) 10 kHz, (k) 15 kHz, and (l) 20 kHz, respectively. (m)−(r) are the harmonic ratios, R35, from samples I−VIII at driving field frequencies of (m) 1 kHz, (n) 3 kHz, (o) 5 kHz, (p) 10 kHz, (q) 15 kHz, and (r) 20 kHz, respectively. The error bar represents the standard deviation from five independent MPS measurements.

respectively. These values are summarized in Tables S1 and S2 in the Supporting Information.

The differences in the harmonics from samples VIII and IX indicate that the rabbit IgG polyclonal antibodies have been successfully anchored onto MNPs. The conjugation of antibodies onto MNPs could slightly increase the hydrodynamic size of MNPs (see Scheme 1(d)), which is also evident in the DLS results in Figure 5(a)−(e) where for Figure 5(d) and (e) the average hydrodynamic sizes are 48.4 and 46.3 nm for negative control groups VIII (MNP+Aby) and IX (bare MNP), respectively.

3.4. Harmonic Ratio (R35) as an MNP Quantity-Independent Metric for the Detection of the H1N1 Nucleoprotein. As the harmonics are largely dependent on the number of MNPs from the sample, the MPS results could be biased by the deviations of MNP quantities from one sample to another, especially for the detection of very low concentration target biomarkers. Besides the metrics of the third and the fifth harmonics for the characterization of H1N1 nucleoproteins, the harmonic ratio, R35, has also been proposed as an MNP quantity-independent metric for the detection of biomarkers (see Notes S7 in the Supporting Information).[27,32,58] Herein, the harmonic ratios (R35) from samples I−IX at various driving field frequencies are summarized in Figure 3(a). Again, a clear trend is noticed that at all driving field frequencies, the samples with higher concentrations of the H1N1 nucleoprotein yield smaller R35 values. Figure 3(a):i−iv highlights the R35 values from each sample at driving field frequencies of 1 kHz, 5 kHz, 10 kHz, and 20 kHz, respectively.

Figure 3(b) shows the boxplot of R35 values from MNP samples at all driving field frequencies. The statistical first quartile (Q1), median (Q2), and third quartile (Q3) R35 values from samples I−IX are summarized in Table 1. Again, there is a clear trend that the R35 value decreases as the concentration of the H1N1 nucleoprotein increases.

3.5. Sensitivity of H1N1 Nucleoprotein Detection. The MPS responses of MNPs versus H1N1 nucleoprotein concentrations ranging from 44 nM to 4.42 μM (amount from 4.4 pmole to 442 pmole) are investigated and shown in Figure 4. Overall, the harmonic amplitudes and the R35 values increase as the concentration of the H1N1 nucleoprotein decreases. Furthermore, neither the third harmonic amplitude nor the fifth harmonic amplitude metrics succeed in distinguishing samples I (4.42 μM) and II (2.21 μM) at the driving field frequency of 20 kHz, where the concentrations of the H1N1 nucleoprotein from these samples are extremely high (see Notes S9 in the Supporting Information). On the other hand, the harmonic ratio, R35, demonstrates comparable capabilities in distinguishing high and low concentrations of H1N1 nucleoprotein samples (see Figure S3(c) in the Supporting Information). However, it fails to detect the differences in samples I (4.42 μM) and II (2.21 μM) at the 20 kHz driving field frequency, either. All the metrics reported in this paper, the third harmonic, the fifth harmonic, and the

https://dx.doi.org/10.1021/acsami.0c00815
ACS Appl. Mater. Interfaces 2020, 12, 13686−13697

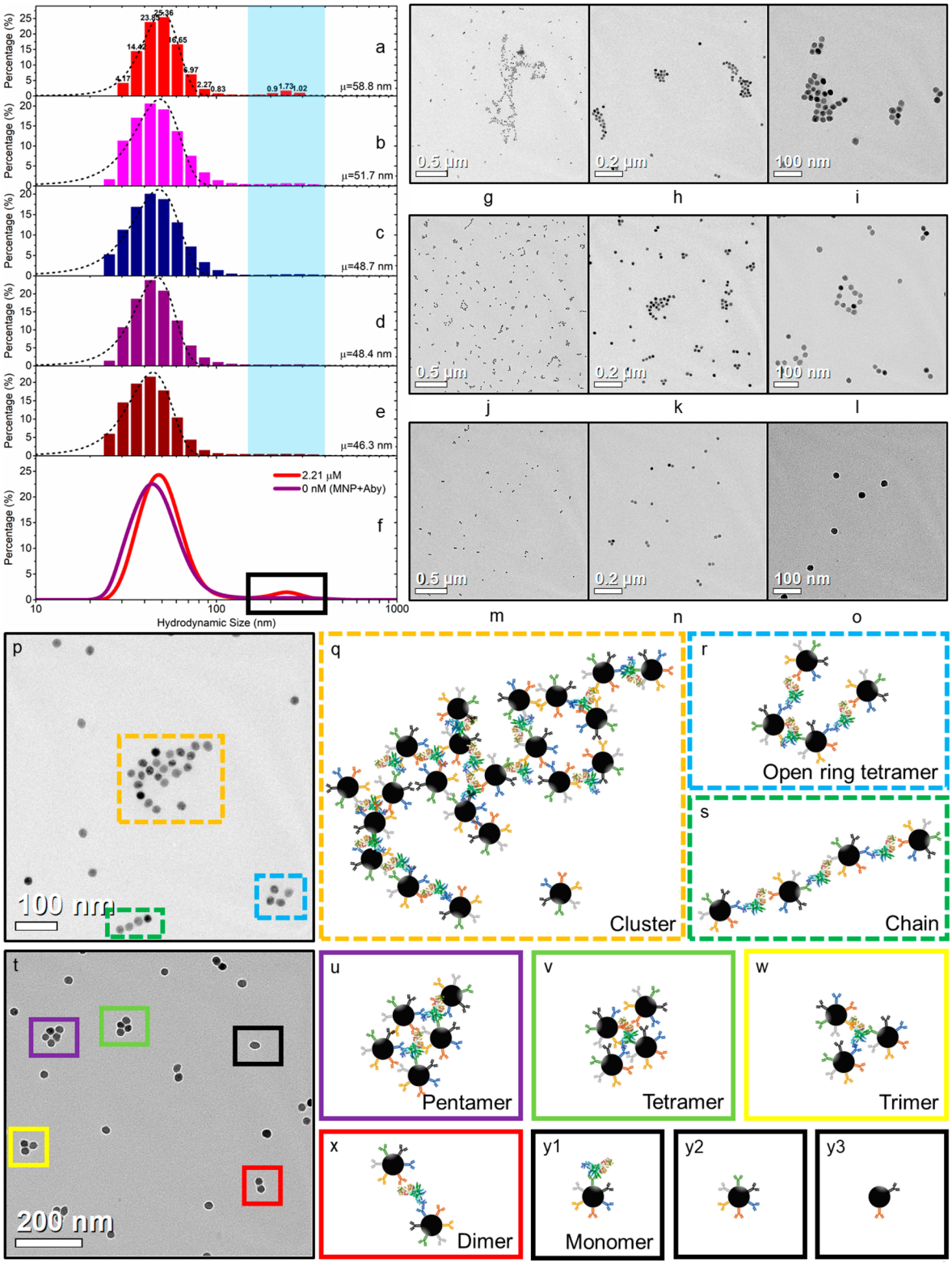

Figure 5. Statistical distribution of the hydrodynamic sizes of samples (a) II, (b) IV, (c) VI, (d) VIII, and (e) IX as characterized by DLS. Dotted lines are the fitted log-normal distribution curves. The μ values represent the statistical mean of the hydrodynamic sizes of the samples. The peaks in the blue highlighted region at the tail show decreasing numbers of MNP self-assemblies from samples II–IV, VI, VIII, and IX. (f) Comparison of the measured DLS size distribution curves between samples II (2.21 μM) and VIII (0 nM, MNP+Aby). The peak at the tail of the DLS size distribution curve from sample II is highlighted in the black square. (g)–(o) are the bright-field TEM images of samples II (g)–(i), VI (j)–(l), and IX (m)–(o). (p) and (t) are the bright-field TEM images from sample VI, highlighting the different shapes of MNP assemblies in the sample. (q), (r), and (s) are the MNP self-assembly models: (q) the classic MNP self-assembly model (cluster); (r) the MNP open ring tetramer model, and (s) the MNP chain model representing the orange, blue, and green dotted contours in (p), respectively. (u), (v), (w), (x), and (y1)–(y3) are the MNP pentamer, tetramer, trimer, dimer, and monomer models representing the purple, lime, yellow, red, and black solid contours in (t), respectively. Note that parts (q)–(s) and (u)–(y) are not drawn to scale.

https://dx.doi.org/10.1021/acsami.0c00815
ACS Appl. Mater. Interfaces 2020, 12, 13686–13697

harmonic ratio R35, are capable of detecting as low as 44 nM (4.4 pmole) H1N1 nucleoprotein.

3.6. Hydrodynamic Size Analysis on the MNP Self-Assemblies. The hydrodynamic sizes of the samples are characterized by Dynamic Light Scatter (DLS, Microtrac NanoFlex). Figure 5(a)−(f) shows the hydrodynamic size distributions of samples II (2.21 μM), IV (442 nM), VI (88 nM), VIII (0 nM, MNP+Aby), and IX (0 nM, bare MNP) with mean values of 58.8 nm, 51.7 nm, 48.7 nm, 48.4 nm, and 46.3 nm, respectively. The decreasing mean values from samples II−IX imply a gradual decrease in the self-assembly degrees of MNPs. Although the primary peaks in the size distributions for all the samples are nearly similar, the main differences come from the peaks at the tails of the size distribution curves (sizes between 200 and 300 nm) which are highlighted in the blue area from Figure 5(a)−(e) as well as the black square in Figure 5(f). The tail shows the largest peak in sample II which gradually diminishes in the consecutive samples with little to no peak in sample IX. The black dashed lines in Figure 5(a)−(e) are the log-normal curve fittings of the particle sizes from samples II, IV, VI, VIII, and IX. Figure 5(f) highlights the differences in the collected DLS size distribution curves from samples II and VIII. Sample II containing 100 μL of 2.21 μM H1N1 nucleoprotein shows the maximum self-assembly degree, and hence the largest mean hydrodynamic size is observed. Decreasing concentration of the H1N1 nucleoprotein in the remaining samples results in less degrees of MNP self-assembly, hence, smaller mean hydrodynamic size. In addition, from Figure 5(f) we also observed that the width of the hydrodynamic size distribution curve increases as the self-assembly degree of MNPs increases. DLS characteristics of these samples show good agreement with the MPS measurements discussed earlier.

3.7. Morphological Characterization on the MNP Self-Assemblies. The morphologies of the MNPs and MNP self-assemblies from samples I−IX are characterized by transmission electron microscopy (TEM, FEI T12 120 kV). Each TEM sample is prepared by dipping a drop of sample fluid onto a TEM grid (TED PELLA, Inc.). The droplet is air-dried at room temperature before taking the TEM characterization. As shown in Figure 5(g)−(o), the bright-field TEM images are taken from samples II (2.21 μM), VI (88 nM), and IX (0 nM, bare MNP). MNPs show an average magnetic core size of around 25 nm and a narrow size distribution, which is critical in obtaining consistent and comparable experimental results. Larger MNP self-assemblies are observed from samples with higher H1N1 nucleoprotein concentration like sample II, which is consistent with the DLS results that higher nucleoprotein concentration yields larger average hydrodynamic size.

It has been mentioned earlier that the H1N1 nucleoprotein molecule has many epitopes that allow the binding of multiple IgG polyclonal antibodies. In addition, the MNPs are surface-functionalized with multiple IgG polyclonal antibodies that would in turn favor the binding to multiple H1N1 nucleoprotein molecules. This cross-linking between MNPs and H1N1 nucleoproteins causes the formation of different degrees of MNP self-assemblies, which has been captured in the TEM images from sample VI as shown in Figure 5(p) and (t) and is schematically drawn in Figure 5(q)−(y3). Figure 5(q), (r), and (s) shows the classic MNP self-assembly (cluster), an open ring tetramer, and a chain tetramer highlighted in the dotted-orange, dotted-blue, and dotted-green contours in Figure 5(p), respectively. Figure 5(u), (v), (w), and (x) shows the formation of a pentamer, a tetramer, a trimer, and a dimer highlighted in solid-purple, solid-lime, solid-yellow, and solid-red contours in Figure 5(t), respectively. The solid-black contour in Figure 5(t) is a monomer, and all possible schematic representations for the formation of monomers are drawn in Figure 5(y1)−(y3). The possible reasons for monomer MNPs, as shown in TEM images, in the presence of H1N1 nucleoproteins are 1) the MNP is conjugated with H1N1 nucleoproteins but is not cross-linked to a second MNP (see Figure 5(y1)); 2) the MNP is not bound to any H1N1 nucleoprotein molecule (see Figure 5(y2)); or 3) the MNP does not have enough IgG polyclonal antibodies anchored on its surface decreasing its ability to bind with H1N1 nucleoprotein molecules and assemble into a cluster (see Figure 5(y3)).

4. CONCLUSION

In this paper, we have successfully demonstrated the feasibility of using the MPS system combined with the self-assembly of MNPs for rapid, sensitive, and wash-free detection of the H1N1 nucleoprotein. The H1N1 nucleoprotein molecule has multiple epitopes that serve as binding sites for IgG polyclonal antibodies. Thus, each H1N1 nucleoprotein may be bound to more than one MNP, consequently assembling into clusters. In addition, each MNP is functionalized with IgG antibodies specific to multiple epitopes of the H1N1 nucleoprotein, which enables the particle to bind to multiple H1N1 nucleoprotein molecules. As a result, the cross-linking of MNPs and H1N1 nucleoproteins leads to different degrees of MNP self-assemblies depending on the number/concentration of H1N1 nucleoprotein molecules in the MNP ferrofluid. Noticeable changes in the macroscopic magnetic responses of MNPs are detected by the MPS system when these ferrofluid samples are subjected to external oscillating magnetic fields. Herein, we have reported the third harmonic, the fifth harmonic, and the harmonic ratio R35 as metrics for the detection of the H1N1 nucleoprotein.

The detection scheme of self-assembly of MNPs along with the harmonic metrics used in this present study was able to detect concentrations as low as 44 nM (4.4 pmole) of the H1N1 nucleoprotein. There are several advantages for using the MPS method: 1) *Rapid*: the testing time for detection is within 10 s; 2) *Sensitive*: detection limits are at the pmole level; 3) *Wash-free*: the as-prepared surface functionalized MNPs can be mixed directly with the fluidic sample without further wash steps, and the analytical signals are detected directly from the entire sample volume, making the bioassays simple and fast; 4) *Easy-to-use*: measurement could be carried out on minimally processed biological samples by nontechnicians with minimum technical training requirements; 5) *Cost effective*: each bioassay only uses nanogram amounts of iron oxide nanoparticles; 6) *Portable:* the entire MPS system could be assembled onto a single PCB board, allowing for the configuration of a hand-held device for field testing. In short, the approach we report here is a rapid and versatile technique that is suitable for the quantitative detection of a wide range of biomarkers/analytes. MPS is a promising, new, and cheap bioassay platform that has the potential to be applied in many biomedical applications including both *in vivo* and *in vitro* diagnostics. Furthermore, a test kit containing microliter volumes of surface functionalized MNPs along with a point-of-care MPS device opens the future

https://dx.doi.org/10.1021/acsami.0c00815
ACS Appl. Mater. Interfaces 2020, 12, 13686−13697

to field-based bioassays in the areas of nanomedicine, food safety, agriculture, and veterinary medicine.

■ ASSOCIATED CONTENT

Supporting Information

The Supporting Information is available free of charge at https://pubs.acs.org/doi/10.1021/acsami.0c00815.

Magnetic particle spectroscopy system setups; magnetic relaxation time models; Langevin model of magnetic responses; phase lag model; induced voltage in pick-up coils; third and fifth harmonics; third over fifth harmonic ratio (R35) as MNP quantity-independent metric; R35 heatmap; capabilities of third harmonic, fifth harmonic, and harmonic ratio R35 as metrics for distinguishing H1N1 nucleoprotein samples with high and low concentrations; Table S1, third harmonic amplitudes (μV) from Figure 2(a):i−iv; Table S2, fifth harmonic amplitudes (μV) from Figure 2(b):v−viii; and Table S3, experimental design of samples I−IX (PDF)

■ AUTHOR INFORMATION

Corresponding Authors

Kai Wu − *Department of Electrical and Computer Engineering, University of Minnesota, Minneapolis, Minnesota 55455, United States;* orcid.org/0000-0002-9444-6112; Email: wuxx0803@umn.edu

Jian-Ping Wang − *Department of Electrical and Computer Engineering, University of Minnesota, Minneapolis, Minnesota 55455, United States*; Email: jpwang@umn.edu

Authors

Jinming Liu − *Department of Electrical and Computer Engineering, University of Minnesota, Minneapolis, Minnesota 55455, United States;* orcid.org/0000-0002-4313-5816

Renata Saha − *Department of Electrical and Computer Engineering, University of Minnesota, Minneapolis, Minnesota 55455, United States;* orcid.org/0000-0002-0389-0083

Diqing Su − *Department of Chemical Engineering and Material Science, University of Minnesota, Minneapolis, Minnesota 55455, United States;* orcid.org/0000-0002-5790-8744

Venkatramana D. Krishna − *Department of Veterinary Population Medicine, University of Minnesota, St. Paul, Minnesota 55108, United States*

Maxim C.-J. Cheeran − *Department of Veterinary Population Medicine, University of Minnesota, St. Paul, Minnesota 55108, United States*

Complete contact information is available at: https://pubs.acs.org/10.1021/acsami.0c00815

Notes

The authors declare no competing financial interest.

■ ACKNOWLEDGMENTS

This study was financially supported in part by the Institute of Engineering in Medicine of the University of Minnesota through FY18 IEM Seed Grant Funding Program and the College of Veterinary Medicine Emerging, Zoonotic and Infectious Diseases Signature Program, USDA-NIFA SAES General Agriculture research funds (MIN-62-097). Portions of this work were conducted in the Minnesota Nano Center, which is supported by the National Science Foundation through the National Nano Coordinated Infrastructure Network (NNCI) under Award Number ECCS-1542202. Portions of this work were carried out in the Characterization Facility, University of Minnesota, a member of the NSF-funded Materials Research Facilities Network (www.mrfn.org) via the MRSEC program.

■ REFERENCES

(1) Taubenberger, J. K.; Morens, D. M. 1918 Influenza: The Mother of All Pandemics. *Rev. Biomed.* **2006**, *17* (1), 69−79.

(2) Kumar, B.; Asha, K.; Khanna, M.; Ronsard, L.; Meseko, C. A.; Sanicas, M. The Emerging Influenza Virus Threat: Status and New Prospects for Its Therapy and Control. *Arch. Virol.* **2018**, *163* (4), 831−844.

(3) Influenza (Seasonal). World Health Organization. https://www.who.int/news-room/fact-sheets/detail/influenza-(seasonal) (accessed 2020-03-12).

(4) Albo, C.; Valencia, A.; Portela, A. Identification of an RNA Binding Region within the N-Terminal Third of the Influenza A Virus Nucleoprotein. *J. Virol.* **1995**, *69* (6), 3799−3806.

(5) Arranz, R.; Coloma, R.; Chichón, F. J.; Conesa, J. J.; Carrascosa, J. L.; Valpuesta, J. M.; Ortín, J.; Martín-Benito, J. The Structure of Native Influenza Virion Ribonucleoproteins. *Science* **2012**, *338* (6114), 1634−1637.

(6) Moeller, A.; Kirchdoerfer, R. N.; Potter, C. S.; Carragher, B.; Wilson, I. A. Organization of the Influenza Virus Replication Machinery. *Science* **2012**, *338* (6114), 1631−1634.

(7) Ruigrok, R. W.; Baudin, F. Structure of Influenza Virus Ribonucleoprotein Particles. II. Purified RNA-Free Influenza Virus Ribonucleoprotein Forms Structures That Are Indistinguishable from the Intact Influenza Virus Ribonucleoprotein Particles. *J. Gen. Virol.* **1995**, *76* (4), 1009−1014.

(8) Shu, L.; Bean, W.; Webster, R. Analysis of the Evolution and Variation of the Human Influenza A Virus Nucleoprotein Gene from 1933 to 1990. *J. Virol.* **1993**, *67* (5), 2723−2729.

(9) Portela, A.; Digard, P. The Influenza Virus Nucleoprotein: A Multifunctional RNA-Binding Protein Pivotal to Virus Replication. *J. Gen. Virol.* **2002**, *83* (4), 723−734.

(10) Leirs, K.; Tewari Kumar, P.; Decrop, D.; Pérez-Ruiz, E.; Leblebici, P.; Van Kelst, B.; Compernolle, G.; Meeuws, H.; Van Wesenbeeck, L.; Lagatie, O. Bioassay Development for Ultrasensitive Detection of Influenza a Nucleoprotein Using Digital ELISA. *Anal. Chem.* **2016**, *88* (17), 8450−8458.

(11) Storch, G. A. Rapid Diagnostic Tests for Influenza. *Curr. Opin. Pediatr.* **2003**, *15* (1), 77−84.

(12) Pang, Y.; Rong, Z.; Wang, J.; Xiao, R.; Wang, S. A Fluorescent Aptasensor for H5N1 Influenza Virus Detection Based-on the Core−Shell Nanoparticles Metal-Enhanced Fluorescence (MEF). *Biosens. Bioelectron.* **2015**, *66*, 527−532.

(13) Ganzenmueller, T.; Kluba, J.; Hilfrich, B.; Puppe, W.; Verhagen, W.; Heim, A.; Schulz, T.; Henke-Gendo, C. Comparison of the Performance of Direct Fluorescent Antibody Staining, a Point-of-Care Rapid Antigen Test and Virus Isolation with That of RT-PCR for the Detection of Novel 2009 Influenza A (H1N1) Virus in Respiratory Specimens. *J. Med. Microbiol.* **2010**, *59* (6), 713−717.

(14) Li, Z.-N.; Weber, K. M.; Limmer, R. A.; Horne, B. J.; Stevens, J.; Schwerzmann, J.; Wrammert, J.; McCausland, M.; Phipps, A. J.; Hancock, K. Evaluation of Multiplex Assay Platforms for Detection of Influenza Hemagglutinin Subtype Specific Antibody Responses. *J. Virol. Methods* **2017**, *243*, 61−67.

(15) Faccini, S.; De Mattia, A.; Chiapponi, C.; Barbieri, I.; Boniotti, M. B.; Rosignoli, C.; Franzini, G.; Moreno, A.; Foni, E.; Nigrelli, A. D. Development and Evaluation of a New Real-Time RT-PCR Assay for Detection of Proposed Influenza D Virus. *J. Virol. Methods* **2017**, *243*, 31−34.

(16) Chartrand, C.; Leeflang, M. M. G.; Minion, J.; Brewer, T.; Pai, M. Accuracy of Rapid Influenza Diagnostic Tests A Meta-Analysis. *Ann. Intern. Med.* **2012**, *156* (7), 500−U80.

(17) Merckx, J.; Wali, R.; Schiller, I.; Caya, C.; Gore, G. C.; Chartrand, C.; Dendukuri, N.; Papenburg, J. Diagnostic Accuracy of Novel and Traditional Rapid Tests for Influenza Infection Compared With Reverse Transcriptase Polymerase Chain Reaction A Systematic Review and Meta-Analysis. *Ann. Intern. Med.* **2017**, *167* (6), 394−409.
(18) González-Del Vecchio, M.; Catalán, P.; de Egea, V.; Rodríguez-Borlado, A.; Martos, C.; Padilla, B.; Rodríguez-Sanchez, B.; Bouza, E. An Algorithm to Diagnose Influenza Infection: Evaluating the Clinical Importance and Impact on Hospital Costs of Screening with Rapid Antigen Detection Tests. *Eur. J. Clin. Microbiol. Infect. Dis.* **2015**, *34* (6), 1081−1085.
(19) Cruz, A. T.; Demmler-Harrison, G. J.; Caviness, A. C.; Buffone, G. J.; Revell, P. A. Performance of a Rapid Influenza Test in Children during the H1N1 2009 Influenza A Outbreak. *Pediatrics* **2010**, *125* (3), No. e645.
(20) Wu, K.; Klein, T.; Krishna, V. D.; Su, D.; Perez, A. M.; Wang, J.-P. Portable GMR Handheld Platform for the Detection of Influenza A Virus. *ACS Sens.* **2017**, *2*, 1594−1601.
(21) Krishna, V. D.; Wu, K.; Perez, A. M.; Wang, J. P. Giant Magnetoresistance-Based Biosensor for Detection of Influenza A Virus. *Front. Microbiol.* **2016**, *7*, 400.
(22) Su, D.; Wu, K.; Krishna, V.; Klein, T.; Liu, J.; Feng, Y.; Perez, A. M.; Cheeran, M. C.; Wang, J.-P. Detection of Influenza a Virus in Swine Nasal Swab Samples With a Wash-Free Magnetic Bioassay and a Handheld Giant Magnetoresistance Sensing System. *Front. Microbiol.* **2019**, *10*, 1077.
(23) Wu, K.; Su, D.; Saha, R.; Wong, D.; Wang, J.-P. Magnetic Particle Spectroscopy-Based Bioassays: Methods, Applications, Advances, and Future Opportunities. *J. Phys. D: Appl. Phys.* **2019**, *52*, 173001.
(24) Krause, H.-J.; Wolters, N.; Zhang, Y.; Offenhäusser, A.; Miethe, P.; Meyer, M. H.; Hartmann, M.; Keusgen, M. Magnetic Particle Detection by Frequency Mixing for Immunoassay Applications. *J. Magn. Magn. Mater.* **2007**, *311*, 436−444.
(25) Nikitin, P. I.; Vetoshko, P. M.; Ksenevich, T. I. New Type of Biosensor Based on Magnetic Nanoparticle Detection. *J. Magn. Magn. Mater.* **2007**, *311*, 445−449.
(26) Wu, K.; Schliep, K.; Zhang, X.; Liu, J.; Ma, B.; Wang, J. Characterizing Physical Properties of Superparamagnetic Nanoparticles in Liquid Phase Using Brownian Relaxation. *Small* **2017**, *13*, 1604135.
(27) Zhang, X.; Reeves, D. B.; Perreard, I. M.; Kett, W. C.; Griswold, K. E.; Gimi, B.; Weaver, J. B. Molecular Sensing with Magnetic Nanoparticles Using Magnetic Spectroscopy of Nanoparticle Brownian Motion. *Biosens. Bioelectron.* **2013**, *50*, 441−446.
(28) Wu, K.; Liu, J.; Wang, Y.; Ye, C.; Feng, Y.; Wang, J.-P. Superparamagnetic Nanoparticle-Based Viscosity Test. *Appl. Phys. Lett.* **2015**, *107*, No. 053701.
(29) Rauwerdink, A. M.; Hansen, E. W.; Weaver, J. B. Nanoparticle Temperature Estimation in Combined Ac and Dc Magnetic Fields. *Phys. Med. Biol.* **2009**, *54*, L51.
(30) Perreard, I.; Reeves, D.; Zhang, X.; Kuehlert, E.; Forauer, E.; Weaver, J. Temperature of the Magnetic Nanoparticle Microenvironment: Estimation from Relaxation Times. *Phys. Med. Biol.* **2014**, *59*, 1109.
(31) Orlov, A. V.; Khodakova, J. A.; Nikitin, M. P.; Shepelyakovskaya, A. O.; Brovko, F. A.; Laman, A. G.; Grishin, E. V.; Nikitin, P. I. Magnetic Immunoassay for Detection of Staphylococcal Toxins in Complex Media. *Anal. Chem.* **2013**, *85*, 1154−1163.
(32) Wu, K.; Liu, J.; Su, D.; Saha, R.; Wang, J.-P. Magnetic Nanoparticle Relaxation Dynamics-Based Magnetic Particle Spectroscopy for Rapid and Wash-Free Molecular Sensing. *ACS Appl. Mater. Interfaces* **2019**, *11* (26), 22979−22986.
(33) Perez, J. M.; O'Loughin, T.; Simeone, F. J.; Weissleder, R.; Josephson, L. DNA-Based Magnetic Nanoparticle Assembly Acts as a Magnetic Relaxation Nanoswitch Allowing Screening of DNA-Cleaving Agents. *J. Am. Chem. Soc.* **2002**, *124* (12), 2856−2857.
(34) Miao, P.; Tang, Y.; Wang, L. DNA Modified Fe3O4@ Au Magnetic Nanoparticles as Selective Probes for Simultaneous Detection of Heavy Metal Ions. *ACS Appl. Mater. Interfaces* **2017**, *9* (4), 3940−3947.
(35) Mezger, A.; Fock, J.; Antunes, P.; Østerberg, F. W.; Boisen, A.; Nilsson, M.; Hansen, M. F.; Ahlford, A.; Donolato, M. Scalable DNA-Based Magnetic Nanoparticle Agglutination Assay for Bacterial Detection in Patient Samples. *ACS Nano* **2015**, *9* (7), 7374−7382.
(36) Chinen, A. B.; Guan, C. M.; Ferrer, J. R.; Barnaby, S. N.; Merkel, T. J.; Mirkin, C. A. Nanoparticle Probes for the Detection of Cancer Biomarkers, Cells, and Tissues by Fluorescence. *Chem. Rev.* **2015**, *115* (19), 10530−10574.
(37) Li, Y.; Lin, R.; Wang, L.; Huang, J.; Wu, H.; Cheng, G.; Zhou, Z.; MacDonald, T.; Yang, L.; Mao, H. PEG-b-AGE Polymer Coated Magnetic Nanoparticle Probes with Facile Functionalization and Anti-Fouling Properties for Reducing Non-Specific Uptake and Improving Biomarker Targeting. *J. Mater. Chem. B* **2015**, *3* (17), 3591−3603.
(38) Klein, T.; Wang, W.; Yu, L.; Wu, K.; Boylan, K. L.; Vogel, R. I.; Skubitz, A. P.; Wang, J.-P. Development of a Multiplexed Giant Magnetoresistive Biosensor Array Prototype to Quantify Ovarian Cancer Biomarkers. *Biosens. Bioelectron.* **2019**, *126*, 301−307.
(39) Liu, J.; Wu, K.; Wang, J.-P. Magnetic Properties of Cubic FeCo Nanoparticles with Anisotropic Long Chain Structure. *AIP Adv.* **2016**, *6* (5), No. 056126.
(40) Liu, J.; Schliep, K.; He, S.-H.; Ma, B.; Jing, Y.; Flannigan, D. J.; Wang, J.-P. Iron Nanoparticles with Tunable Tetragonal Structure and Magnetic Properties. *Phys. Rev. Mater.* **2018**, *2* (5), No. 054415.
(41) Thanh, N. T. *Clinical Applications of Magnetic Nanoparticles: From Fabrication to Clinical Applications*; CRC Press: 2018.
(42) Orlov, A. V.; Bragina, V. A.; Nikitin, M. P.; Nikitin, P. I. Rapid Dry-Reagent Immunomagnetic Biosensing Platform Based on Volumetric Detection of Nanoparticles on 3D Structures. *Biosens. Bioelectron.* **2016**, *79*, 423−429.
(43) Wang, Y.; Zhu, G.; Qi, W.; Li, Y.; Song, Y. A Versatile Quantitation Platform Based on Platinum Nanoparticles Incorporated Volumetric Bar-Chart Chip for Highly Sensitive Assays. *Biosens. Bioelectron.* **2016**, *85*, 777−784.
(44) Tian, B.; Liao, X.; Svedlindh, P.; Strömberg, M.; Wetterskog, E. Ferromagnetic Resonance Biosensor for Homogeneous and Volumetric Detection of DNA. *ACS Sens.* **2018**, *3* (6), 1093−1101.
(45) Schrittwieser, S.; Pelaz, B.; Parak, W. J.; Lentijo-Mozo, S.; Soulantica, K.; Dieckhoff, J.; Ludwig, F.; Guenther, A.; Tschöpe, A.; Schotter, J. Homogeneous Biosensing Based on Magnetic Particle Labels. *Sensors* **2016**, *16* (6), 828.
(46) Luo, Y.; Alocilja, E. C. Portable Nuclear Magnetic Resonance Biosensor and Assay for a Highly Sensitive and Rapid Detection of Foodborne Bacteria in Complex Matrices. *J. Biol. Eng.* **2017**, *11* (1), 14.
(47) Castro, C. M.; Ghazani, A. A.; Chung, J.; Shao, H.; Issadore, D.; Yoon, T.-J.; Weissleder, R.; Lee, H. Miniaturized Nuclear Magnetic Resonance Platform for Detection and Profiling of Circulating Tumor Cells. *Lab Chip* **2014**, *14* (1), 14−23.
(48) Zhao, Y.; Li, Y.; Jiang, K.; Wang, J.; White, W. L.; Yang, S.; Lu, J. Rapid Detection of Listeria Monocytogenes in Food by Biofunctionalized Magnetic Nanoparticle Based on Nuclear Magnetic Resonance. *Food Control* **2017**, *71*, 110−116.
(49) Jackman, L. M.; Sternhell, S. *Application of Nuclear Magnetic Resonance Spectroscopy in Organic Chemistry: International Series in Organic Chemistry*; Elsevier: 2013.
(50) Park, K.; Harrah, T.; Goldberg, E. B.; Guertin, R. P.; Sonkusale, S. Multiplexed Sensing Based on Brownian Relaxation of Magnetic Nanoparticles Using a Compact AC Susceptometer. *Nanotechnology* **2011**, *22* (8), No. 085501.
(51) Chieh, J.-J.; Huang, K.-W.; Lee, Y.-Y.; Wei, W.-C. Dual-Imaging Model of SQUID Biosusceptometry for Locating Tumors Targeted Using Magnetic Nanoparticles. *J. Nanobiotechnol.* **2015**, *13* (1), 11.
(52) Trisnanto, S. B.; Kitamoto, Y. Optimizing Coil System for Magnetic Susceptometer with Widely-Adjustable Field-Strength and Frequency. *Jpn. J. Appl. Phys.* **2016**, *55* (2S), No. 02BD02.

https://dx.doi.org/10.1021/acsami.0c00815
ACS Appl. Mater. Interfaces 2020, 12, 13686−13697

(53) Achtsnicht, S.; Pourshahidi, A. M.; Offenhäusser, A.; Krause, H.-J. Multiplex Detection of Different Magnetic Beads Using Frequency Scanning in Magnetic Frequency Mixing Technique. *Sensors* **2019**, *19* (11), 2599.
(54) Wang, W.; Ma, P.; Dong, H.; Krause, H.-J.; Zhang, Y.; Willbold, D.; Offenhaeusser, A.; Gu, Z. A Magnetic Nanoparticles Relaxation Sensor for Protein−Protein Interaction Detection at Ultra-Low Magnetic Field. *Biosens. Bioelectron.* **2016**, *80*, 661−665.
(55) Nikitin, M.; Orlov, A.; Znoyko, S.; Bragina, V.; Gorshkov, B.; Ksenevich, T.; Cherkasov, V.; Nikitin, P. Multiplex Biosensing with Highly Sensitive Magnetic Nanoparticle Quantification Method. *J. Magn. Magn. Mater.* **2018**, *459*, 260−264.
(56) Nikitin, M. P.; Orlov, A.; Sokolov, I.; Minakov, A.; Nikitin, P.; Ding, J.; Bader, S.; Rozhkova, E.; Novosad, V. Ultrasensitive Detection Enabled by Nonlinear Magnetization of Nanomagnetic Labels. *Nanoscale* **2018**, *10* (24), 11642−11650.
(57) Khurshid, H.; Shi, Y.; Berwin, B. L.; Weaver, J. B. Evaluating Blood Clot Progression Using Magnetic Particle Spectroscopy. *Med. Phys.* **2018**, *45* (7), 3258−3263.
(58) Rauwerdink, A. M.; Weaver, J. B. Harmonic Phase Angle as a Concentration-Independent Measure of Nanoparticle Dynamics. *Med. Phys.* **2010**, *37*, 2587−2592.

https://dx.doi.org/10.1021/acsami.0c00815
ACS Appl. Mater. Interfaces 2020, 12, 13686−13697